Mathematics

http://www.aimspress.com/journal/Math

AIMS Mathematics, 10(9): 22598–22621.
DOI:10.3934/math.20251006
Received: 05 August 2025
Revised: 09 September 2025
Accepted: 12 September 2025
Published: 29 September 2025

Research article

Intelligent forecasting of monkeypox spread using fractional epidemiological models and machine learning

Saeed M. Alamry*

Department of Mathematics and Statistics, College of Science, Taif University, P. O. Box 11099, Taif 21944, Saudi Arabia

* **Correspondence:** Email: sm.alamri@tu.edu.sa.

Abstract: This study develops a fractal-fractional epidemiological model to investigate the transmission dynamics of monkeypox. The existence, uniqueness, and stability of the model are established using fixed-point and Ulam-Hyers frameworks. A fractional Adams-Bashforth scheme is implemented for a numerical approximation, and simulations illustrate the role of memory and fractal effects in the disease spread. To enhance the predictive capability, the model is integrated with an Artificial Neural Network (ANN) and evaluated using publicly available datasets of outbreaks. Benchmarking against Caputo-derivative-based models demonstrates that the proposed approach achieves a superior goodness-of-fit, parameter identifiability, and short-term forecasting accuracy. These results highlight the potential of fractal-fractional modeling combined with machine learning to improve forecasting and inform control strategies for emerging epidemics.

Keywords: monkeypox transmission modeling; existence and uniqueness analysis; fractal-fractional derivative; Adams-Bashforth numerical scheme; neural network-based simulation
Mathematics Subject Classification: 34D20, 34K20, 34K60, 92C60, 92D45

---

1. Introduction

Monkeypox is a zoonotic viral infection caused by the monkeypox virus, which belongs to the Poxviridae family, and has recently gained attention as a significant global health issue. Initially detected in laboratory monkeys in 1958 [1], the disease later manifested in humans, with the first case documented in the Democratic Republic of Congo in 1970 [2]. Genetically, the virus shares close similarities with the variola virus, which is responsible for smallpox. Historically, monkeypox outbreaks have been primarily restricted to regions of Central and West Africa and have generally been limited in scale and localized in nature [3]. However, recent years have witnessed a significant rise in monkeypox cases, with outbreaks reported in numerous countries worldwide, including non-endemic regions [4].

The recent outbreak, which was marked by clusters of cases occurring in both endemic and non-endemic regions, has become a significant global health concern. In response, the World Health Organization (WHO) classified it as a public health emergency of international concern and stressed the importance of prompt measures to curb its spread [5]. Transmission typically occurs through direct contact with infected animals or humans and can also result from exposure to contaminated objects [6]. Clinical symptoms of monkeypox resemble those of smallpox, thereby presenting with fever, headaches, muscle pain, and skin rashes; however, monkeypox is distinct in causing lymph node enlargement [7]. While no standardized treatment is currently available, vaccination against smallpox can provide partial protection against monkeypox [8, 9].

A thorough understanding of monkeypox transmission dynamics is essential to design and implement effective control measures. To address this, various mathematical modeling approaches have been employed to examine the disease spread, thereby considering key factors such as transmission pathways, vaccine efficacy, and the influence of different intervention strategies [10, 11]. These models have shed light on the potential for outbreaks, the importance of early detection and isolation, and the need for robust public health interventions to mitigate the impact of this re-emerging infectious disease.

The re-emergence of monkeypox in 2022 has sparked renewed interest in understanding and controlling this viral zoonotic disease. While research on monkey pox transmission dynamics has been ongoing, the application of fractional-order operators to model the spread of monkey pox remains relatively unexplored. However, recent studies have begun to address this gap. For instance, Recent efforts have addressed this research gap through various fractional modeling approaches. For example, Mesady et al. [12] proposed a monkeypox model formulated with the Caputo derivative to analyze the equilibrium behavior, compute the basic reproduction number, and assess the stability properties. Similarly, Qurashi et al. [13] introduced a model that incorporated the Atangana-Baleanu (AB) operator, with an emphasis on equilibrium stability. In another study, Peter et al. [25] explored the dynamics and control mechanisms of monkeypox transmission using the Caputo-Fabrizio derivative.

Fractional differential systems are widely used to model real-world phenomena, though exact analytical solutions remain challenging. Therefore, numerical schemes such as Adams-Bashforth, Newton polynomial, and predictor-corrector methods [14–16] are commonly employed. In epidemiology, their relevance is evident: Giudici [17] emphasized safe machine learning for predictive health modeling, Jan et al. [18] applied a fractal-fractional Caputo model to Rift Valley fever, and Moya and Rodrigues [19] modeled HIV prophylaxis using fractional calculus. These studies motivate our use of fractal-fractional operators with neural networks for monkeypox modeling.

The fractal-fractional (FF) operator, although relatively new, is powerful in capturing memory effects and fractal properties through the fractional order (α) and fractal dimension (η), features that are especially relevant in biological systems. Moreover, recent advances demonstrate the synergy between fractional calculus and neural networks: Shafqat and Alsaadi [20] modeled rabies with ANNs, Turab et al. [21] applied a Caputo-based ANN framework to hepatitis B, Shafqat et al. [22] studied alcoholism with fractional order, Abuasbeh et al. [23] analyzed COVID-19 with delay Caputo operators, and Al-Quran et al. [24] investigated poliomyelitis using fractional derivatives and deep neural networks. Collectively, these works confirm the value of hybrid fractional-ANN approaches and reinforce our motivation for applying them to monkeypox transmission.

The dynamics of the compartments described in the model [25] are formulated through the following system of nonlinear differential equations:

$$\begin{cases} \dfrac{dD_h}{dt} = \theta_h - \dfrac{(\beta_1 I_r + \beta_2 I_h)S_h}{N_h} - \mu_h S_h + \phi Q_h, \\ \dfrac{dE_h}{dt} = \dfrac{(\beta_1 I_r + \beta_2 I_h)S_h}{N_h} - (\alpha_1 + \alpha_2 + \mu_h)E_h, \\ \dfrac{dI_h}{dt} = \alpha_1 E_h - (\mu_h + \delta_h + \gamma)I_h, \\ \dfrac{dQ_h}{dt} = \alpha_2 E_h - (\phi + \tau + \delta_h + \mu_h)Q_h, \\ \dfrac{dR_h}{dt} = \gamma I_h + \tau Q_h - \mu_h R_h, \\ \dfrac{dS_r}{dt} = \theta_r - \dfrac{\beta_3 S_r I_r}{N_r} - \mu_r S_r, \\ \dfrac{dE_r}{dt} = \dfrac{\beta_3 S_r I_r}{N_r} - (\mu_r + \alpha_3)E_r, \\ \dfrac{dI_r}{dt} = \alpha_3 E_r - (\mu_r + \delta_r)I_r. \end{cases} \tag{1.1}$$

Fractional systems are particularly well-suited for modeling biological systems due to their ability to incorporate memory and hereditary properties, which are essential to understand complex biological behaviors. The memory function enables fractional models to integrate past information in more accurate predictions and interpretations. This research examines how memory affects moneypox dynamics by employing a model formulated using fractional differential systems. It is important to note that derivatives of non-integer order can be represented in multiple forms. Riemann provided the earliest formulation, followed by Liouville, and then Caputo in 1967, whose definition is widely applied today. Both these formulations involve singular kernels, which often introduce challenges in numerical. To address these limitations, Caputo and Fabrizio [26] proposed an alternative approach that employed an exponential kernel instead of a singular one. Subsequently, Atangana and Baleanu [27] extended this concept by incorporating the Mittag-Leffler function in place of the exponential kernel. These developments have shown that the modified derivatives exhibit several notable characteristics [28, 29].

Model formulation

Building upon the framework presented in [25], we propose an enhanced mathematical model designed to capture the transmission dynamics of the virus between individuals while incorporating a compartment for immune individuals, which was absent in the original formulation. To achieve a more flexible and accurate description of the system, we employ a fractal-fractional derivative in the Caputo sense, which offers significant advantages for modeling complex dynamical behaviors. The proposed model extends the previous work by introducing arbitrary fractional-order derivatives, with $0 < \alpha \leq 1$, alongside a fractal dimension parameter $0 < \eta \leq 1$, to better account for memory and hereditary effects in disease progression. The population is structured into six distinct compartments: susceptible (H_S), exposed (H_E), infected (H_A), hospitalized (H_Q), recovered (H_R), and immune individuals (H_V). The total population size is represented as follows:

$$N(t) = H_S(t) + H_E(t) + H_A(t) + H_Q(t) + H_R(t) + H_V(t).$$

Recruitment into the susceptible class occurs at a constant rate ξ, while natural mortality is denoted by ξ_1. The transmission of infection from infected individuals to susceptibles is characterized by the rate ξ_2. Recovery dynamics are governed by ξ_3 for infected individuals and ξ_6 for those hospitalized. Additional parameters include ξ_5 for disease-induced mortality, and ξ_4 for the transition from the infected to hospitalized compartment. A schematic representation of the model's structure is illustrated in Figure 1. The following governing system of equations is formulated using fractional-order operators to reflect the memory properties inherent in epidemiological processes:

$$\begin{cases} {}^{FF}\mathbf{D}_t^{\alpha,\eta} H_S(t) = \xi - \xi_2 \dfrac{H_A H_S}{N} - \xi_1 H_S, \\ {}^{FF}\mathbf{D}_t^{\alpha,\eta} H_E(t) = \xi_2 \dfrac{H_A H_S}{N} - (\xi + \xi_1) H_E, \\ {}^{FF}\mathbf{D}_t^{\alpha,\eta} H_A(t) = \xi_9 H_E - (\xi_3 + \xi_4 + \xi_1 + \xi_5) H_A, \\ {}^{FF}\mathbf{D}_t^{\alpha,\eta} H_Q(t) = \xi_4 H_A - (\xi_6 + \xi_5 + \xi_1) H_Q, \\ {}^{FF}\mathbf{D}_t^{\alpha,\eta} H_R(t) = \xi_6 H_Q + \xi_3 H_A - \xi_1 H_R, \\ {}^{FF}\mathbf{D}_t^{\alpha,\eta} H_V(t) = \xi\eta - \xi_1 H_V, \\ H_S(0) = H_{S_0} \geq 0, \ \ H_E(0) = H_{E_0} \geq 0, \ \ H_A(0) = H_{A_0} \geq 0, \ \ H_Q(0) = H_{Q_0} \geq 0, \ \ H_R(0) = H_{R_0} \geq 0, \\ \ H_V(0) = H_{V_0} \geq 0, \ \ 0 < \alpha, \eta \leq 1. \end{cases} \tag{1.2}$$

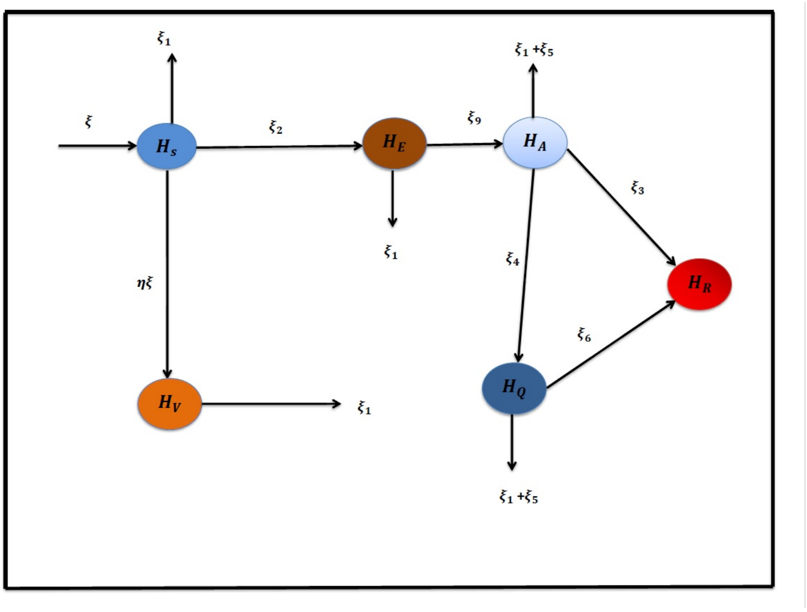

Figure 1. Flowchart of the monkeypox model.

The analysis in this work focuses on Eq (1.2), thereby employing the fractal-fractional derivative due to its ability to deliver more realistic results and provide greater flexibility compared to integer-order derivatives. The model is formulated with a fractional order α and fractal dimension η, which allows the dynamics to capture the behavior between two integer limits. This approach ensures that the population densities of all compartments converge rapidly, particularly at lower derivative orders.

The construction of model (1.2) is motivated by the underlying biological kinetics of monkeypox transmission and progression. First, disease transmission and recovery exhibit memory effects, since the probability of infection or recovery at a given time depends not only on the present state but also on the history of exposure, incubation, and treatment. Fractional derivatives are well-suited to capture such hereditary processes because their kernels incorporate the system's past states into present dynamics. Second, real-world populations exhibit heterogeneous and fractal-like contact patterns, rather than uniform mixing. Fractal-fractional derivatives offer an additional degree of freedom through the fractal dimension parameter, thus enabling the model to represent irregular interaction structures and multiscale behaviors within the host population.

Taken together, the use of a fractal-fractional operator is not a simple substitution of integer-order derivatives. Instead, it is grounded in the mechanistic reality that

1) Infection progression is history-dependent,
2) Immunity and hospitalization involve delays with memory effects, and
3) Contact and transmission patterns often display fractal scaling.

Therefore, the operator provides a biologically meaningful and mathematically flexible tool to better represent monkeypox epidemiology compared to classical integer-order models.

The structure of the paper is as follows: Section 2 introduces the fundamental concepts and theoretical preliminaries. In Section 3, we establish the existence and uniqueness results using the Banach fixed-point framework. Section 4 presents the numerical methodology based on the well-known Adams-Bashforth technique for solve the proposed model, and numerical simulations are conducted in MATLAB to provide graphical illustrations and facilitate an interpretation of the results. Finally, the concluding remarks are summarized in Section 6.

2. Basic results

Definition 2.1. [30] Let $\mathcal{U}(t)$ be a function defined on the interval (a, b) that is continuous and differentiable of order η. The Riemann-Liouville form that incorporate a Power-Law kernel leads to the definition of the fractal-fractional derivative as follows:

$$ {}^{FF}\mathbf{D}_t^{\alpha,\eta}(\mathcal{U}(t)) = \frac{1}{(p-\alpha)}\frac{d}{dt^\eta}\int_0^t (t-x)^{p-\alpha-1}\mathcal{U}(x)\,dx, \tag{2.1} $$

where $p-1 < \alpha, \eta \leq p$, with $p \in \mathbb{N}$. The derivative is expressed as $\dfrac{d\mathcal{U}(x)}{dx^\alpha} = \lim\limits_{t\to 0}\dfrac{\mathcal{U}(t)-\mathcal{U}(x)}{t^\eta - x^\eta}$.

Definition 2.2. [30] If $\mathcal{U}(t)$ is continuous on (a, b), then its fractal-fractional order integral of order α using the Power-Law kernel is given by the followig:

$$ {}^{FF}\mathbf{I}^{\alpha}\mathcal{U}(t) = \frac{\eta}{\Gamma(\alpha)}\int_0^t (t-x)^{\alpha-1}x^{\eta-1}\mathcal{U}(x)\,dx. \tag{2.2} $$

Definition 2.3. The system in (1.2) is said to satisfy Ulam-Hyers stability if there exists a constant $\mathcal{Q}_{\alpha,\eta} \geq 0$ such that for every $\epsilon > 0$ and for all solutions $F \in C^1(\mathcal{X}, \mathbb{R})$, the following inequality holds:

$$|{}^{FF}\mathbf{D}^{\alpha,\eta}F(t) - \Psi(t, F(t))| \leq \epsilon, \quad t \in \mathcal{X}. \tag{2.3}$$

Moreover, $\mathcal{Y} \in C^1(\mathcal{X}, \mathbb{R})$ represents the unique solution of (1.2) and satisfies the following:

$$|F(t) - \mathcal{Y}(t)| \leq \mathcal{Q}_{\alpha,\eta}, \quad t \in \mathcal{X}. \tag{2.4}$$

Notation: For the qualitative study, consider the Banach space $\mathrm{U} = \underbrace{\mathrm{X} \times \mathrm{X} \times \cdots \times \mathrm{X}}_{6 \text{ times}}$ with $\mathrm{X} = C(\mathcal{X})$. The norm is defined by the following:

$$\|F\| = \max_{t\in[0,T]}\{|H_S(t)| + |H_E(t)| + |H_A(t)| + |H_Q(t)| + |H_R(t)| + |H_V(t)|\}.$$

3. Theoretical results of model (1.2)

In this section, we focus on establishing the existence of solutions for the model (1.2). As the considered integral is differentiable, the right-hand side of system (1.2) can be reformulated as follows:

$$\begin{aligned}
{}^{\mathcal{RL}}\mathbf{D}^{\alpha}H_S(t) &= \eta t^{\eta-1}\mathcal{Y}_1(H_S, H_E, H_A, H_Q, H_R, H_V, t) = \xi - \xi_2\frac{H_AH_S}{N} - \xi_1H_S,\\
{}^{\mathcal{RL}}\mathbf{D}^{\alpha}H_E(t) &= \eta t^{\eta-1}\mathcal{Y}_2(H_S, H_E, H_A, H_Q, H_R, H_V, t) = \xi_2\frac{H_AH_S}{N} - (\xi + \xi_1)H_E,\\
{}^{\mathcal{RL}}\mathbf{D}^{\alpha}H_A(t) &= \eta t^{\eta-1}\mathcal{Y}_3(H_S, H_E, H_A, H_Q, H_R, H_V, t) = \xi_9H_E - (\xi_3 + \xi_4 + \xi_1 + \xi_5)H_A,\\
{}^{\mathcal{RL}}\mathbf{D}^{\alpha}H_Q(t) &= \eta t^{\eta-1}\mathcal{Y}_4(H_S, H_E, H_A, H_Q, H_R, H_V, t) = \xi_4H_A - (\xi_6 + \xi_5 + \xi_1)H_Q,\\
{}^{\mathcal{RL}}\mathbf{D}^{\alpha}H_R(t) &= \eta t^{\eta-1}\mathcal{Y}_5(H_S, H_E, H_A, H_Q, H_R, H_V, t) = \xi_6H_Q + \xi_3H_A - \xi_1H_R,\\
{}^{\mathcal{RL}}\mathbf{D}^{\alpha}H_V(t) &= \eta t^{\eta-1}\mathcal{Y}_6(H_S, H_E, H_A, H_Q, H_R, H_V, t) = \xi\eta - \xi_1H_V.
\end{aligned} \tag{3.1}$$

As a result of (3.1) and for $t \in \mathcal{X}$, the advance model maybe written in the following scheme:

$$\begin{aligned}
{}^{\mathcal{RL}}\mathbf{D}^{\alpha}F(t) &= \eta t^{\eta-1}\Psi(t, F(t)), \quad 0 < \alpha, \eta \leq 1,\\
F(0) &= F_0,
\end{aligned} \tag{3.2}$$

by changing ${}^{\mathcal{RL}}\mathbf{D}^{\alpha,\eta}$ with ${}^{C}\mathbf{D}^{\alpha,\eta}$ and using the integral of Riemann-Liouville sense, the solution of (3.2) is as follows:

$$F(t) = F_0 + \frac{\eta}{\Gamma(\alpha)}\int_0^t x^{\eta-1}(t-x)^{\alpha-1}\Psi(x, F(x))dx, \tag{3.3}$$

where

$$F(t) = \begin{cases} H_S(t)\\ H_E(t)\\ H_A(t)\\ H_Q(t),\\ H_R(t),\\ H_V(t), \end{cases}, \quad F_0 = \begin{cases} H_{S_0}\\ H_{E_0}\\ H_{A_0}\\ H_{Q_0},\\ H_{R_0},\\ H_{V_0}, \end{cases}, \quad \Psi(t, F(t)) = \begin{cases} \mathcal{Y}_1(H_S, H_E, H_A, H_Q, H_R, H_V, t)\\ \mathcal{Y}_2(H_S, H_E, H_A, H_Q, H_R, H_V, t)\\ \mathcal{Y}_3(H_S, H_E, H_A, H_Q, H_R, H_V, t)\\ \mathcal{Y}_4(H_S, H_E, H_A, H_Q, H_R, H_V, t)\\ \mathcal{Y}_5(H_S, H_E, H_A, H_Q, H_R, H_V, t)\\ \mathcal{Y}_6(H_S, H_E, H_A, H_Q, H_R, H_V, t). \end{cases} \tag{3.4}$$

Next, we reformulate the system (1.2) as a fixed-point problem by introducing the operator $\mathcal{T} : \mathbf{V} \to \mathbf{V}$, which is expressed as follows:

$$\mathcal{T}(F)(t) = F_0 + \frac{\eta}{\Gamma(\alpha)} \int_0^t x^{\eta-1}(t-x)^{\alpha-1}\Psi(x, F(x))\, dx. \tag{3.5}$$

The existence of solutions for the proposed model can be established using the following theorem [31].

Theorem 3.1. Consider a mapping $\mathcal{T} : \mathbf{V} \to \mathbf{V}$ that is completely continuous. Define

$$\mathcal{J}(\mathcal{T}) = \{F \in \mathbf{V} : F = \nu\mathcal{T}(F),\ \nu \in [0, 1]\}.$$

If this set is bounded, then $\mathcal{T}$ admits at least one fixed point in $\mathbf{V}$.
To establish our results, we assume the following condition:

(E) There exists a positive constant $\mathcal{A}_\Psi > 0$ such that for any $F, \bar{F} \in \mathbf{V}$, the inequality

$$|\Psi(t, F) - \Psi(t, \bar{F})| \leq \mathcal{A}_\Psi\, |F - \bar{F}|$$

holds for all t in the considered domain.

For convenience, we introduce the following notation:

$$\hbar = \frac{\eta\, T^{\alpha+\eta-1}\, \mathscr{B}(\alpha, \eta)}{\Gamma(\alpha)}, \tag{3.6}$$

where $\mathscr{B}(\alpha, \eta)$ denotes the Beta function.

Theorem 3.2. Assume that the mapping $\Psi : \mathcal{G} \times \mathbf{V} \to \mathbb{R}$ is continuous and satisfies condition **(E)**. Under these assumptions, the fractional-order model described in (1.2) admits at least one solution.

Proof. Assume that $\mathcal{H} \subset \mathbf{V}$ is a bounded set. By the definition of $\mathcal{H}$, we have the following:

$$|\Psi(t, F(t))| \leq Q_\Psi, \quad \text{for some } Q_\Psi > 0, \text{ and for all } F \in \mathcal{H}.$$

Hence, for each $F \in \mathcal{H}$, the following estimate holds:

$$\begin{aligned} \|\mathcal{T}(F)\| &\leq \frac{\eta Q_\Psi}{\Gamma(\alpha)} \max_{t\in[0,T]} \int_0^t (t-x)^{\alpha-1} x^{\eta-1}\, dx \\ &\leq \hbar Q_\Psi, \end{aligned}$$

which shows that the operator $\mathcal{T}$ is uniformly bounded.

Next, we prove the continuity of $\mathcal{T} : \mathbf{V} \to \mathbf{V}$ as defined in (3.5). Consider a sequence $\{F_n\}$ in $\mathbf{V}$ such that $F_n \to F$ as $n \to \infty$. For any $t \in [0, T]$, we compute the following:

$$\begin{aligned} \|\mathcal{T}(F_n) - \mathcal{T}(F)\| &\leq \frac{\eta}{\Gamma(\wp)} \max_{t\in[0,T]} \int_0^t (t-x)^{\alpha-1} x^{\eta-1} \left|\Psi(x, F_n(x)) - \Psi(x, F(x))\right| dx \\ &\leq \frac{\eta\mathcal{A}_\Psi T^{\alpha+\eta-1}\mathscr{B}(\alpha, \eta)}{\Gamma(\alpha)} \|F_n - F\|, \end{aligned} \tag{3.7}$$

where $\mathcal{A}_\Psi$ is the Lipschitz constant. Since $\|F_n - F\| \to 0$, the operator $\mathcal{T}$ is continuous.

To establish equi-continuity, consider any $t_1, t_2 \in [0, T]$. Then,

$$\begin{aligned}\|\mathcal{T}(F(t_1)) - \mathcal{T}(F(t_2))\| &\leq \frac{\eta Q_\Psi}{\Gamma(\alpha)}\left|\int_0^{t_1} (t_1 - x)^{\alpha-1} x^{\eta-1}\, dx - \int_0^{t_2} (t_2 - x)^{\alpha-1} x^{\eta-1}\, dx\right| \\ &\leq \frac{\eta Q_\Psi \mathscr{B}(\alpha, \eta)}{\Gamma(\alpha)} (t_1^{\alpha+\eta-1} - t_2^{\alpha+\eta-1}) \to 0 \text{ as } t_1 \to t_2.\end{aligned}$$

Thus, $\mathcal{T}$ is equi-continuous. Consequently, by the Arzelà-Ascoli theorem, $\mathcal{T}$ is compact and completely continuous.

Finally, consider the set $\mathscr{D} = \{F \in \mathbf{V} : \delta\mathcal{T}(F), \delta \in [0, 1]\}$. For any $F \in \mathscr{D}$ and $t \in [0, T]$, we have

$$|F| \leq \hbar Q_\Psi,$$

which shows that $\mathscr{D}$ is bounded. Hence, by Theorem 3.2, the model (1.2) possesses at least one solution. □

In the following theorem, we demonstrate the uniqueness of the solution by applying the Banach contraction principle [31].

Theorem 3.3. Under assumption (**E**), if $\Upsilon < 1$, then the system in (1.2) admits a unique solution, where

$$\Upsilon = \frac{\eta\, Q_\Psi\, T^{\alpha+\eta-1}}{\Gamma(\alpha)} \mathscr{B}(\wp, \eta). \tag{3.8}$$

Proof. Assume that $\max_{t\in[0,T]} |\Psi(t, 0)| = \mathcal{K}_\Psi < \infty$. If the radius r satisfies

$$r \geq \frac{\hbar \mathcal{K}_\Psi}{1 - \hbar Q_\Psi}, \tag{3.9}$$

then $\mathcal{T}(\mathcal{B}_r) \subseteq \mathcal{B}_r$, where $\mathcal{B}_r = \{F \in \mathbf{V} : \|F\| \leq r\}$. For any $F \in \mathcal{B}_r$, we obtain the following:

$$\begin{aligned}\|\mathcal{T}(F)\| &\leq \frac{\eta}{\Gamma(\alpha)} \max_{t\in[0,T]} \int_0^t x^{\eta-1}(t - x)^{\alpha-1}(|\Psi(x, F(x)) - \Psi(x, 0)| + |\Psi(x, 0)|)\, dx \\ &\leq \frac{\eta T^{\alpha+\eta-1} \mathscr{B}(\alpha, \eta)(\mathcal{A}_\Psi\|F\| + \mathcal{K}_\Psi)}{\Gamma(\alpha)} \\ &\leq \hbar(\mathcal{A}_\Psi r + \mathcal{K}_\Psi) \leq r.\end{aligned}$$

Now, let $\mathcal{T} : \mathbf{V} \to \mathbf{V}$ be given by (3.5). Under assumption (**E**), for all $t \in [0, T]$ and $F, \overline{F} \in \mathbf{V}$, we have the following:

$$\begin{aligned}\|\mathcal{T}(F) - \mathcal{T}(\overline{F})\| &\leq \frac{\eta}{\Gamma(\alpha)} \max_{t\in[0,T]} \left|\int_0^t x^{\eta-1}(t - x)^{\alpha-1}\Psi(x, F(x))\, dx - \int_0^t x^{\eta-1}(t - x)^{\alpha-1}\Psi(x, \overline{F}(x))\, dx\right| \\ &\leq \Upsilon_\Psi\|F - \overline{F}\|.\end{aligned} \tag{3.10}$$

Since $\Upsilon_\Psi < 1$, the operator $\mathcal{T}$ is a contraction. Hence, by the Banach fixed-point theorem, the system (1.2) admits a unique solution. □

To investigate the Ulam–Hyers stability of the system (1.2), let us consider a perturbation function $\psi \in \mathcal{Q}(\mathcal{G})$ with the property $\psi(0) = 0$. Assume that the perturbation is bounded such that

- $|\psi(t)| < \varepsilon$, for some small $\varepsilon > 0$,
- the perturbed form of the system is given by:

$$ {}^{FF}\mathbf{D}_t^{\alpha,\eta} F(t) = \Psi(t, F(t)) + \psi(t). $$

Hence, the corresponding perturbed system becomes:

$$ \begin{aligned} {}^{FF}\mathbf{D}_t^{\alpha,\eta} F(t) &= \Psi(t, F(t)) + \psi(t), \\ F(0) &= F_0 \end{aligned} \tag{3.11} $$

satisfies the given relation

$$ \left| F(t) - \left(F_0 + \frac{\eta}{\Gamma(\alpha)} \int_0^t x^{\eta-1} (t-x)^{\alpha-1} \Psi(x, F(x)) dx \right) \right| \leq \hbar\epsilon. \tag{3.12} $$

The corresponding solution of the perturbed system (3.11) can be expressed as follows:

$$ F(t) = F_0 + \frac{\eta}{\Gamma(\alpha)} \int_0^t x^{\eta-1} (t-x)^{\alpha-1} \Big[\Psi(x, F(x)) + \psi(x) \Big] dx. \tag{3.13} $$

By applying the bound $|\psi(t)| \leq \varepsilon$ in (3.13), the required inequality corresponding to relation (3.12) is derived. Consequently, the Ulam–Hyers stability condition for the original system (1.2) is formulated as follows.

Theorem 3.4. Assume that condition (**E**) together with relation (3.12) is satisfied and $\Upsilon_\Psi < 1$, where Υ_Ψ is defined in (3.8). Under these circumstances, the solution of the integral system (1.2) exhibits Ulam-Hyers stability.

Proof. Consider two solutions $(\mathcal{Z}, \mathcal{Z}_1) \in \mathbf{V}$ of system (3.3). By applying the fractal-fractional integral formulation given in (2.2), we can estimate the following:

$$ \begin{aligned} |\mathcal{Z}_1(t) - \mathcal{Z}(t)| &= \left| \mathcal{Z}_1(t) - \left(\mathcal{Z}_0 + \frac{\eta}{\Gamma(\alpha)} \int_0^t (t-x)^{\alpha-1} x^{\eta-1} \Psi(x, \mathcal{Z}(x)) dx \right) \right| \\ &\leq \left| \mathcal{Z}_1(t) - \left(\mathcal{Z}_0 + \frac{\eta}{\Gamma(\alpha)} \int_0^t (t-x)^{\alpha-1} x^{\eta-1} \Psi(x, \mathcal{Z}_1(x)) dx \right) \right| \\ &+ \left| \left(\mathcal{Z}_0 + \frac{\varsigma}{\Gamma(\alpha)} \int_0^t (t-x)^{\alpha-1} x^{\eta-1} \Psi(x, \mathcal{Z}_1(x)) dx \right) \right. \\ &- \left. \left(\mathcal{Z}_0 + \frac{\eta}{\Gamma(\alpha)} \int_0^t (t-x)^{\alpha-1} x^{\eta-1} \Psi(x, \mathcal{Z}(x)) dx \right) \right| \\ &\leq \hbar\epsilon + \Upsilon_\Psi \|\mathcal{Z}_1 - \mathcal{Z}\|. \end{aligned} $$

Thus, it follows that

$$ \|\mathcal{Z}_1 - \mathcal{Z}\| \leq \left(\frac{\hbar}{1 - \Upsilon_\Psi} \right) \epsilon. \tag{3.14} $$

Hence, from inequality (3.14), we conclude that system (3.3), and consequently model (1.2), exhibits Ulam-Hyers stability. □

4. Numerical scheme

In this section, the numerical approximation of the fractal-fractional system is carried out using the fractional Adams-Bashforth scheme, which has been widely applied to solve fractional differential equations due to its stability and convergence properties [14–16]. This approach combines discretization with Lagrange polynomial interpolation, thus making it suitable to capture the hereditary and memory effects intrinsic to fractional operators. For the numerical procedure, Eq (3.3) corresponding to the model is reformulated into the following representation:

$$\begin{cases} {}^{FF}\mathbf{D}_t^{\alpha,\eta} H_S(t) = \xi - \xi_2 \dfrac{H_A H_S}{N} - \xi_1 H_S, \\ {}^{FF}\mathbf{D}_t^{\alpha,\eta} H_E(t) = \xi_2 \dfrac{H_A H_S}{N} - (\xi + \xi_1) H_E, \\ {}^{FF}\mathbf{D}_t^{\alpha,\eta} H_A(t) = \xi_9 H_E - (\xi_3 + \xi_4 + \xi_1 + \xi_5) H_A, \\ {}^{FF}\mathbf{D}_t^{\alpha,\eta} H_Q(t) = \xi_4 H_A - (\xi_6 + \xi_5 + \xi_1) H_Q, \\ {}^{FF}\mathbf{D}_t^{\alpha,\eta} H_R(t) = \xi_6 H_Q + \xi_3 H_A - \xi_1 H_R, \\ {}^{FF}\mathbf{D}_t^{\alpha,\eta} H_V(t) = \xi \eta - \xi_1 H_V. \end{cases} \tag{4.1}$$

Next, we present the numerical approximation of system (4.1) using the discretization at the point $t_{\gamma+1}$. The initial component of the scheme is expressed as follows:

$$H_{S_{\gamma+1}} = H_{S_0} + \frac{\eta}{\Gamma(\alpha)} \int_0^{t_{\gamma+1}} x^{\eta-1} (t_{\gamma+1} - x)^{\alpha-1} \mathcal{Y}_1(H_S, H_E, H_A, H_Q, H_R, H_V, x)\, dx. \tag{4.2}$$

To numerically evaluate the above integral, it is partitioned over subintervals, which results in the following:

$$H_{S_{\gamma+1}} = H_{S_0} + \frac{\eta}{\Gamma(\alpha)} \sum_{\beta=0}^{k} \int_{t_\beta}^{t_{\beta+1}} x^{\eta-1} (t_{\gamma+1} - x)^{\alpha-1} \mathcal{Y}_1(H_S, H_E, H_A, H_Q, H_R, H_V, x)\, dx. \tag{4.3}$$

Within each subinterval $[t_\beta, t_{\beta+1}]$, $\mathcal{Y}_1$ is approximated using Lagrange interpolation polynomials. With a step size $\hbar = t_\beta - t_{\beta-1}$, the term $H^\star_{S_\gamma}$ can be written as follows:

$$\begin{aligned} H^\star_{S_\gamma} \approx \frac{1}{\hbar} \Big[& (t - t_{\beta-1})\, t_\beta^{\eta-1} \mathcal{Y}_1(H_{S_\beta}, H_{E_\beta}, H_{A_\beta}, H_{Q_\beta}, H_{R_\beta}, H_{V_\beta}, t_\beta) \\ & - (t - t_\beta)\, t_{\beta-1}^{\eta-1} \mathcal{Y}_1(H_{S_{\beta-1}}, H_{E_{\beta-1}}, H_{A_{\beta-1}}, H_{Q_{\beta-1}}, H_{R_{\beta-1}}, H_{V_{\beta-1}}, t_{\beta-1}) \Big]. \end{aligned} \tag{4.4}$$

By substituting (4.4) into (4.3), we rewrite as follows:

$$H_{S_{\gamma+1}} = H_{S_0} + \frac{\eta}{\Gamma(\alpha)} \sum_{\beta=0}^{\gamma} \int_{t_\beta}^{t_{\beta+1}} x^{\eta-1} (t_{\gamma+1} - x)^{\alpha-1} H^\star_{S_\gamma}\, dx. \tag{4.5}$$

Finally, simplifying the integral on the right-hand side of (4.5) yields an iterative numerical scheme the $\mathcal{N}_h$ class in (1.2), which utilizes fractal-fractional derivatives as follows:

$$\begin{aligned}H_{S_{\gamma+1}} &= H_{S_0} + \frac{\eta\hbar^{\alpha}}{\Gamma(\alpha+2)}\sum_{\beta=0}^{\gamma}\Big[t_{\beta}^{\eta-1}\mathcal{Y}_1(H_{S_\beta}, H_{E_\beta}, H_{A_\beta}, H_{Q_\beta}, H_{R_\beta}, H_{V_\beta}, t_\beta)\\ &\times\Big((\gamma+1-\beta)^{\eta}(\gamma-\beta+2+\eta)-(\gamma-\beta)^{\eta}(\gamma-\beta+2+2\eta)\Big)\\ &-t_{\beta-1}^{\eta-1}\mathcal{Y}_1(H_{S_{\beta-1}}, H_{E_{\beta-1}}, H_{A_{\beta-1}}, H_{Q_{\beta-1}}, H_{R_{\beta-1}}, H_{V_{\beta-1}}, t_{\beta-1})\\ &\times\Big((\gamma+1-\beta)^{\eta}+1-(\gamma-\beta)^{\eta}(k-\beta+1+\eta)\Big)\Big]. \end{aligned} \tag{4.6}$$

Following the same procedure, the expressions for the remaining components can be derived as follows:

$$\begin{aligned}H_{E_{\gamma+1}} &= H_{E_0} + \frac{\eta\hbar^{\alpha}}{\Gamma(\alpha+2)}\sum_{\beta=0}^{\gamma}\Big[t_{\beta}^{\eta-1}\mathcal{Y}_2(H_{S_\beta}, H_{E_\beta}, H_{A_\beta}, H_{Q_\beta}, H_{R_\beta}, H_{V_\beta}, t_\beta)\\ &\times\Big((\gamma+1-\beta)^{\eta}(\gamma-\beta+2+\eta)-(\gamma-\beta)^{\eta}(\gamma-\beta+2+2\eta)\Big)\\ &-t_{\beta-1}^{\eta-1}\mathcal{Y}_2(H_{S_{\beta-1}}, H_{E_{\beta-1}}, H_{A_{\beta-1}}, H_{Q_{\beta-1}}, H_{R_{\beta-1}}, H_{V_{\beta-1}}, t_{\beta-1})\\ &\times\Big((\gamma+1-\beta)^{\eta}+1-(\gamma-\beta)^{\eta}(k-\beta+1+\eta)\Big)\Big], \end{aligned} \tag{4.7}$$

$$\begin{aligned}H_{A_{\gamma+1}} &= H_{A_0} + \frac{\eta\hbar^{\alpha}}{\Gamma(\alpha+2)}\sum_{\beta=0}^{\gamma}\Big[t_{\beta}^{\eta-1}\mathcal{Y}_3(H_{S_\beta}, H_{E_\beta}, H_{A_\beta}, H_{Q_\beta}, H_{R_\beta}, H_{V_\beta}, t_\beta)\\ &\times\Big((\gamma+1-\beta)^{\eta}(\gamma-\beta+2+\eta)-(\gamma-\beta)^{\eta}(\gamma-\beta+2+2\eta)\Big)\\ &-t_{\beta-1}^{\eta-1}\mathcal{Y}_3(H_{S_{\beta-1}}, H_{E_{\beta-1}}, H_{A_{\beta-1}}, H_{Q_{\beta-1}}, H_{R_{\beta-1}}, H_{V_{\beta-1}}, t_{\beta-1})\\ &\times\Big((\gamma+1-\beta)^{\eta}+1-(\gamma-\beta)^{\eta}(k-\beta+1+\eta)\Big)\Big], \end{aligned} \tag{4.8}$$

$$\begin{aligned}H_{Q_{\gamma+1}} &= H_{Q_0} + \frac{\eta\hbar^{\alpha}}{\Gamma(\alpha+2)}\sum_{\beta=0}^{\gamma}\Big[t_{\beta}^{\eta-1}\mathcal{Y}_4(H_{S_\beta}, H_{E_\beta}, H_{A_\beta}, H_{Q_\beta}, H_{R_\beta}, H_{V_\beta}, t_\beta)\\ &\times\Big((\gamma+1-\beta)^{\eta}(\gamma-\beta+2+\eta)-(\gamma-\beta)^{\eta}(\gamma-\beta+2+2\eta)\Big)\\ &-t_{\beta-1}^{\eta-1}\mathcal{Y}_4(H_{S_{\beta-1}}, H_{E_{\beta-1}}, H_{A_{\beta-1}}, H_{Q_{\beta-1}}, H_{R_{\beta-1}}, H_{V_{\beta-1}}, t_{\beta-1})\\ &\times\Big((\gamma+1-\beta)^{\eta}+1-(\gamma-\beta)^{\eta}(k-\beta+1+\eta)\Big)\Big], \end{aligned} \tag{4.9}$$

$$\begin{aligned}H_{R_{\gamma+1}} &= H_{R_0} + \frac{\eta\hbar^{\alpha}}{\Gamma(\alpha+2)}\sum_{\beta=0}^{\gamma}\Big[t_{\beta}^{\eta-1}\mathcal{Y}_5(H_{S_\beta}, H_{E_\beta}, H_{A_\beta}, H_{Q_\beta}, H_{R_\beta}, H_{V_\beta}, t_\beta)\\ &\times\Big((\gamma+1-\beta)^{\eta}(\gamma-\beta+2+\eta)-(\gamma-\beta)^{\eta}(\gamma-\beta+2+2\eta)\Big) \end{aligned}$$

$$
\begin{aligned}
&-t_{\beta-1}^{\eta-1}\mathcal{Y}_5(H_{S_{\beta-1}}, H_{E_{\beta-1}}, H_{A_{\beta-1}}, H_{Q_{\beta-1}}, H_{R_{\beta-1}}, H_{V_{\beta-1}}, t_{\beta-1}) \\
&\times\Big((\gamma+1-\beta)^{\eta} + 1 - (\gamma-\beta)^{\eta}(k-\beta+1+\eta)\Big)\Big],
\end{aligned} \tag{4.10}
$$

$$
\begin{aligned}
H_{V_{\gamma+1}} \;=\; & H_{V_0} + \frac{\eta\hbar^{\alpha}}{\Gamma(\alpha+2)}\sum_{\beta=0}^{\gamma}\Big[t_{\beta}^{\eta-1}\mathcal{Y}_6(H_{S_\beta}, H_{E_\beta}, H_{A_\beta}, H_{Q_\beta}, H_{R_\beta}, H_{V_\beta}, t_\beta) \\
&\times\Big((\gamma+1-\beta)^{\eta}(\gamma-\beta+2+\eta) - (\gamma-\beta)^{\eta}(\gamma-\beta+2+2\eta)\Big) \\
&-t_{\beta-1}^{\eta-1}\mathcal{Y}_6(H_{S_{\beta-1}}, H_{E_{\beta-1}}, H_{A_{\beta-1}}, H_{Q_{\beta-1}}, H_{R_{\beta-1}}, H_{V_{\beta-1}}, t_{\beta-1}) \\
&\times\Big((\gamma+1-\beta)^{\eta} + 1 - (\gamma-\beta)^{\eta}(k-\beta+1+\eta)\Big)\Big].
\end{aligned} \tag{4.11}
$$

5. Simulation results

In this section, we illustrate the dynamic behavior of each compartment based on the proposed fractal-fractional model and the corresponding numerical approach. The simulations are performed using small initial conditions, along with the parameter values listed in Table 1.

Table 1. Parameter values utilized in model (1.2).

Parameter	Description	Value	Source
ξ_2	Transmission rate between an infected and a susceptible human	0.022325	[25]
ξ	Recruitment rate	29.08	[32, 33]
ξ_6	Recovery rate of critically ill individuals	0.036246	[25]
ξ_3	Recovery rate of infected individuals through natural immunity	0.088366	[25]
ξ_4	Progression rate from infection to critical illness	0.5	[25]
ξ_9	Transition rate from exposed to infectious state	0.016744	[25]
ξ_5	Disease-induced mortality rate for Monkeypox	0.003286	[25]
ξ_1	Natural death rate	0.4252912×10^{-4}	[32]
η	Immunity acquisition rate	0.1	[25]
H_S	Initial susceptible population	10,000	[34]
H_E	Initial exposed individuals	100	[34]
H_A	Initial infected individuals	5.86	[34]
H_Q	Initial hospitalized individuals	1.14	[34]
H_R	Initial recovered population	0	[34]
H_V	Initial immune population	10	[34]

Figure 2 illustrates the temporal evolution of all compartments in the proposed fractal-fractional Monkeypox model. The simulations reveal that the susceptible population (H_S) gradually decreases as the infection spreads. At the same time, the exposed class (H_E) shows an initial rise followed by a decline, thus indicating transitions to infection or immunity. The infected compartment (H_A) exhibits a sharp increase after a short latency period, and reaches its peak before progressively declining due to recovery and hospitalization processes. Similarly, the hospitalized class (H_Q) increases but with a smaller amplitude, thus reflecting the relatively lower proportion of severe cases in the population. The recovered population (H_R) steadily increases as patients recover, whereas the immune compartment (H_V) expands due to control measures or natural immunity, thus contributing to system stabilization over time.

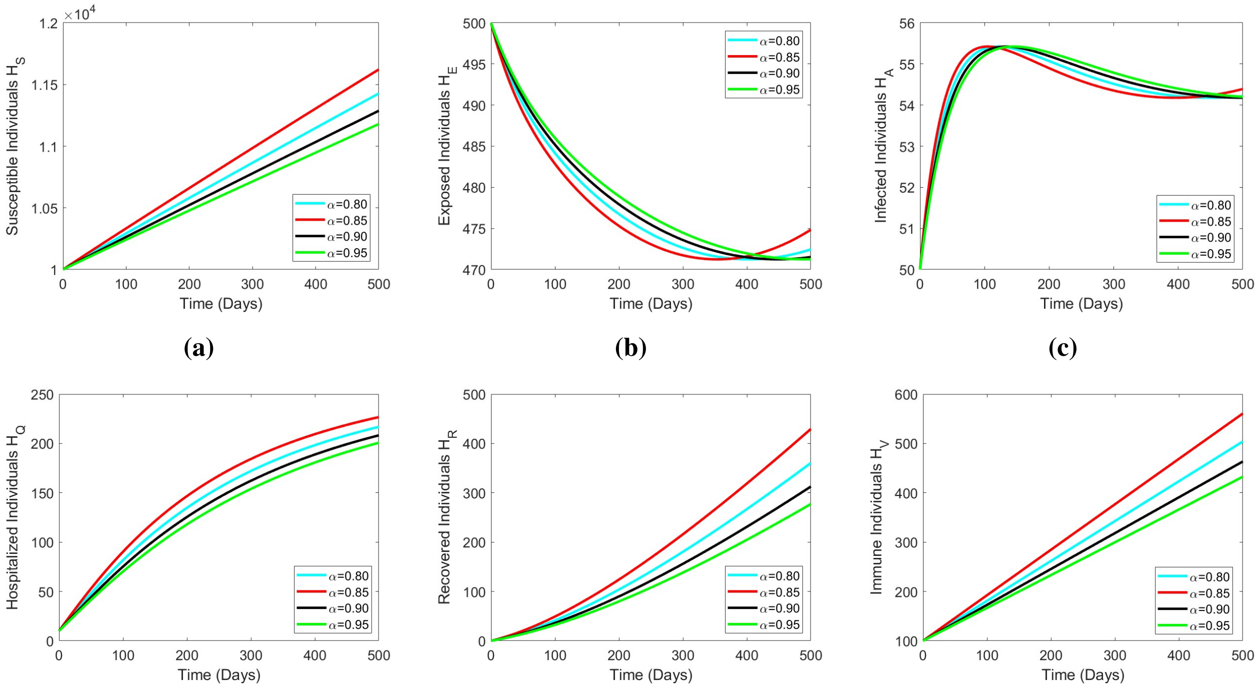

(a) **(b)** **(c)**

(d) **(e)** **(f)**

Figure 2. The graphs of numerical simulation of Female mosquito, Susceptible mosquito, Infected mosquito, Susceptible human, Infected human, and Recovered human.

These numerical findings underscore the importance of the fractal fractional approach, which takes the memory effects and hereditary properties of the system into account. Unlike classical integer-order models, the fractional operator offers a more realistic description of monkeypox transmission dynamics. This characteristic suggests that historical states of infection have a strong influence on future trends, thus making fractional-order modeling particularly effective for long-term forecasting. Furthermore, the results confirm that early interventions such as vaccination and prompt hospitalization play a crucial role in reducing the peak of infection and controlling the overall disease burden.

To ensure transparency and replicability, we provide the detailed configuration of the ANN experiments, which consisted of 3 hidden layers with 50 neurons each, rectified linear unit (ReLU) activation, and a linear output layer. The network was trained using the Adam optimizer with a learning rate of 0.001, a batch size of 64, and the mean squared error (MSE) as the loss function. The dataset was divided into 70% training, 15% validation, and 15% testing subsets. Training was conducted for 1000 epochs, with early stopping based on the validation loss. All experiments and figures were generated using MATLAB R2024a (Deep Learning Toolbox) on a workstation equipped with an Intel i7 CPU (3.2 GHz), 32 GB of RAM, and an NVIDIA RTX 3080 GPU (10 GB). Distinct fractional orders are considered for each partition. Figure 3(a) presents the ANN approach combined with the Adam-Bashforth numerical method. In this approach, numerical solutions generated via the

Adams-Bashforth method serve as training data for the ANN, which subsequently learns the system dynamics and provides the predictive outputs. This hybridization enhances the forecasting accuracy by combining a deterministic numerical approximation with data-driven learning. Similar strategies have been employed in the literature [35], thus confirming the feasibility of such hybrid frameworks.

The performance of the model after 1000 training epochs, which corresponds to a mean squared error of approximately $7.2434e-09$, is illustrated in Figure 3(b). The training progress is shown in Figure 3(c), while Figure 3(d) presents the error histogram, which indicates that the smallest observed error is $-4.5e-05$. Furthermore, Figure 3(e) compares the predicted and actual outputs, thus highlighting the accuracy of the fit for both training and testing datasets. Finally, Figure 3(f) displays the regression analysis for all data subsets, thus confirming that the points closely align with the regression line. This alignment suggests a highly accurate model, with the correlation coefficient R approaching 1.

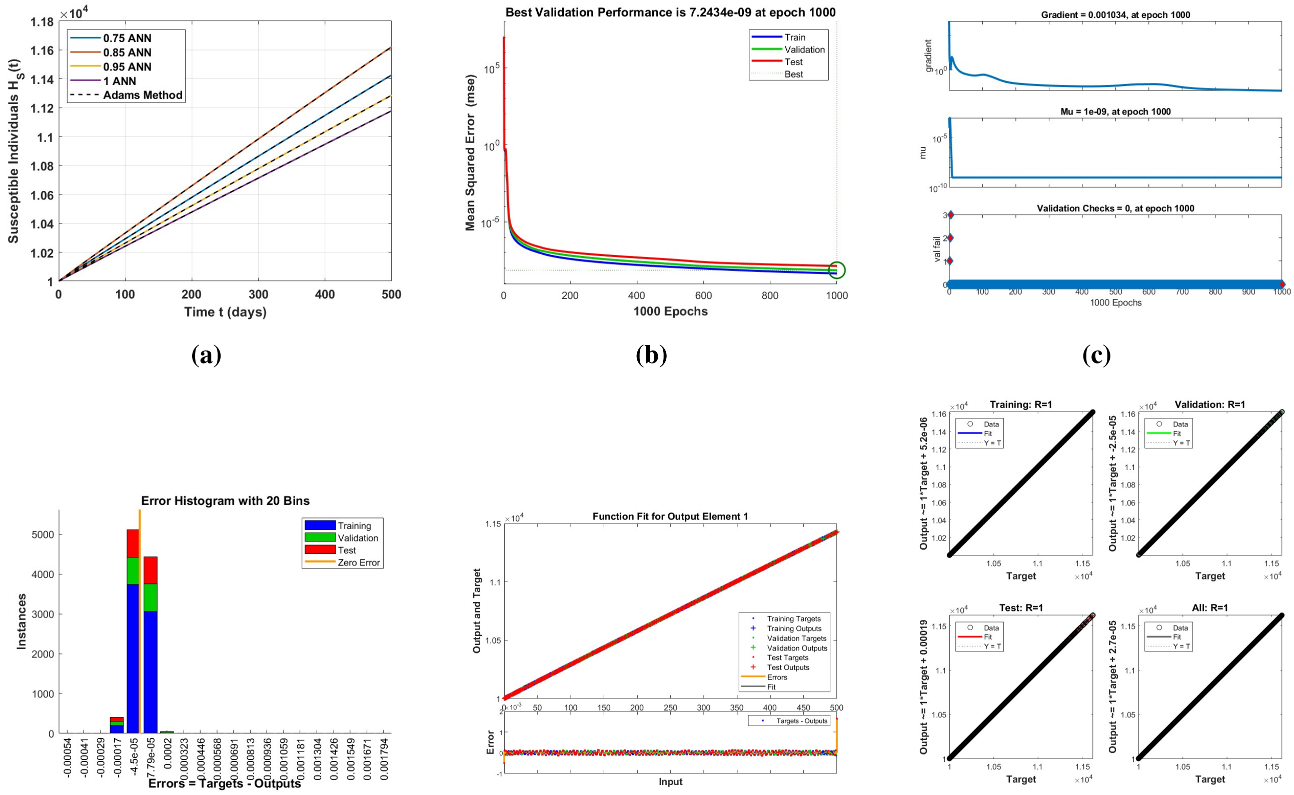

(a) (b) (c)

(d) (e) (f)

Figure 3. Statistical dynamics of the model class H_S: (a) comparison, (b) mean square error, (c) regression, (d)error histogram, (e) training fit, and (f) Regression with ANN.

The ANN strategy, that utilizes the Adam-Bashforth approach, is illustrated in Figure 4(a). Figure 4(b) demonstrates the model's performance at epoch 1000, which achieves a mean square error of $1.1796e-11$. The progression of training is presented in Figure 4(c), while Figure 4(d) depicts an additional view of the training phase. The error distribution is shown in Figure 4(e), where the minimum identified error is approximately $-2.9e-07$. Furthermore, Figure 4(e) includes the comparative accuracy of the training and testing datasets, thus highlighting their respective deviations from the reference values. Finally, the regression outcomes for all datasets, training, validation, and testing, are provided in Figure 4(f). The alignment of data points along the regression line confirms that the final solution is well-trained, with the regression coefficient R approaching unity.

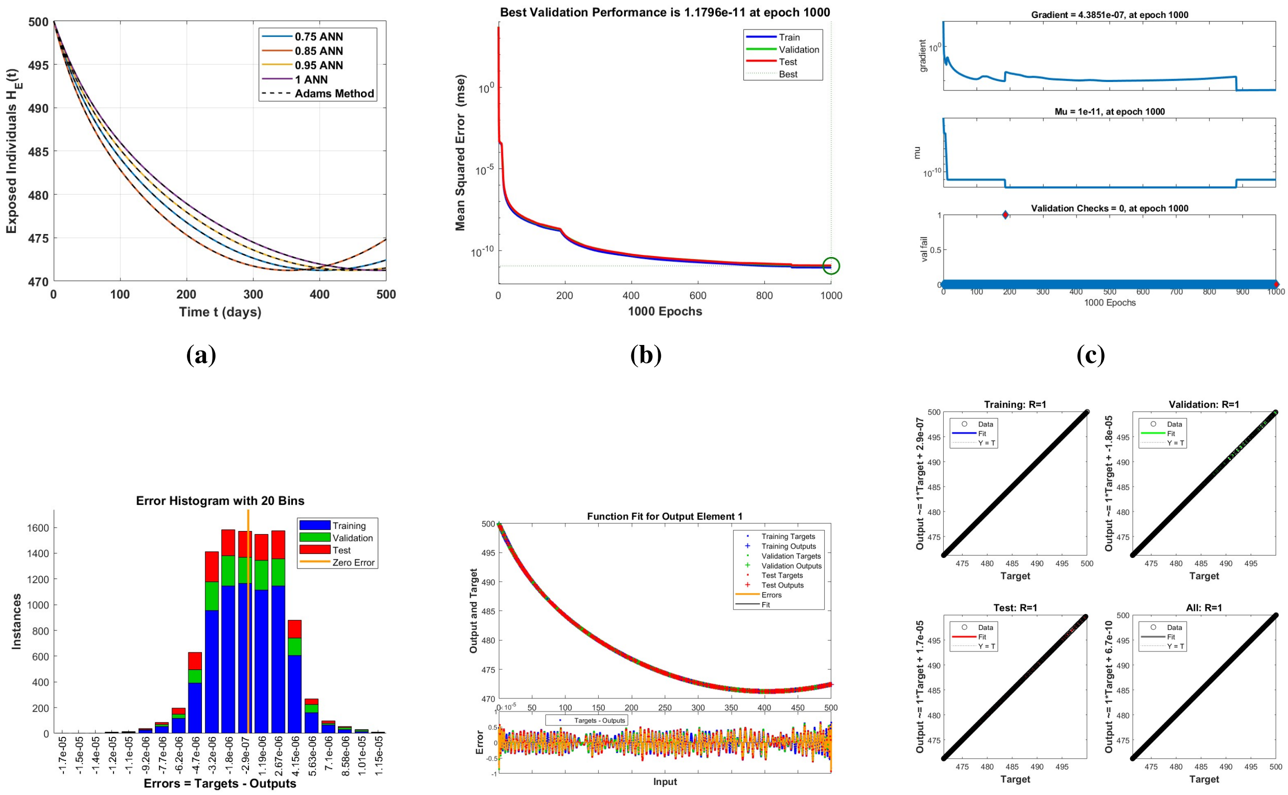

(a) (b) (c)

(d) (e) (f)

Figure 4. Statistical dynamics of the model class H_E: (a) comparison, (b) mean square error, (c) regression, (d)error histogram, (e) training fit, and (f) Regression with ANN.

The ANN strategy that employs the Adam-Bashforth scheme is illustrated in Figure 5(a). The performance of the model at the 541 epoch, is presented in Figure 5(b), and achieves a mean square error of $7.5897e - 11$. Figures 5(b) and 5(d) depict the progression of the training phase. The error distribution, where the lowest error value observed is $-2e - 06$, is shown in Figure 5(d). Furthermore, Figure 5(e) illustrates the comparative accuracy of the training and testing datasets, along with their associated deviations. Finally, the regression analysis for all categories (that is training and testing) is provided in Figure 5(f). The alignment of data points along the regression line confirms that the model achieves an accurate training, with a correlation coefficient R approximately equal to 1.

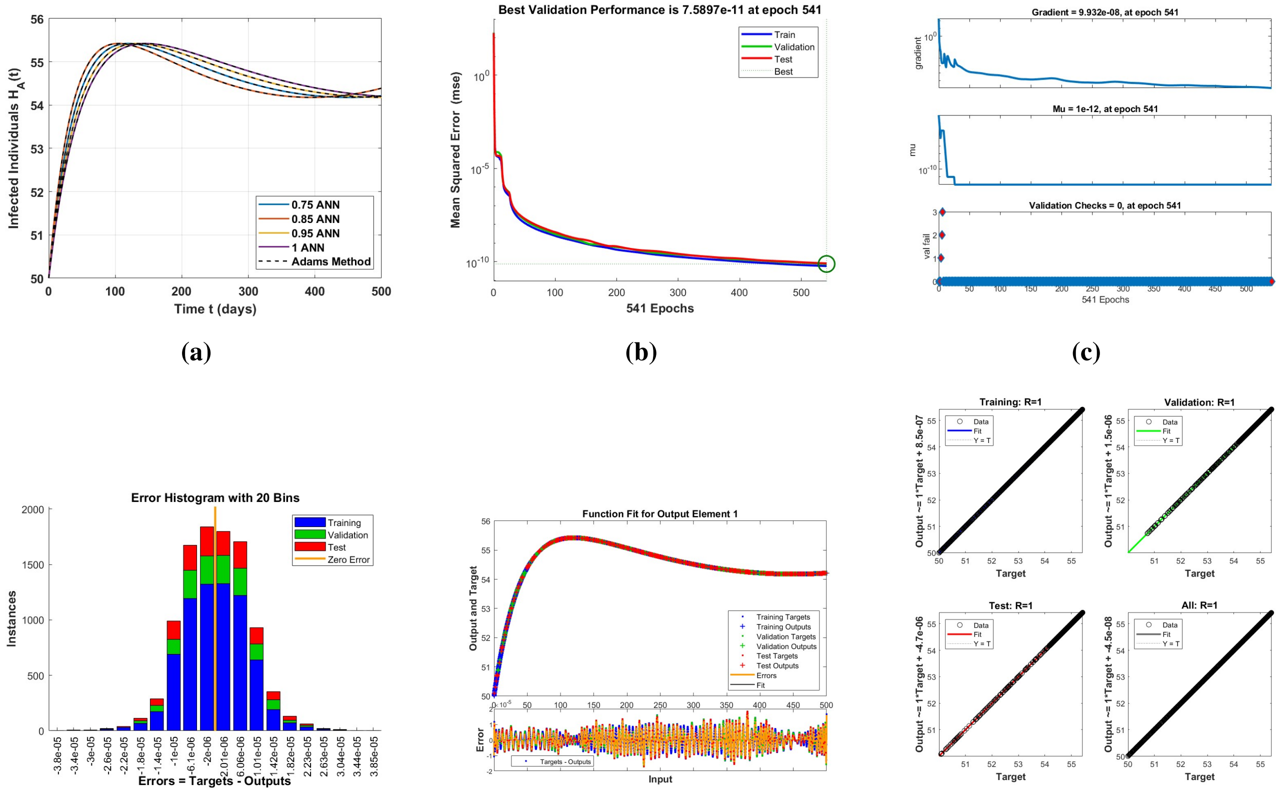

(a) **(b)** **(c)**

(d) **(e)** **(f)**

Figure 5. Statistical dynamics of the model class H_A: (a) comparison, (b) mean square error, (c) regression, (d)error histogram, (e) training fit, and (f) Regression with ANN.

The implementation of the ANN approach, the Adam-Bashforth technique, is presented in Figure 6(a). The model's performance at the 1000 epoch is shown in Figure 6(b) and achieves a mean square error of $1.0185e-09$. Figures 6(c) and 6(d) illustrate the progression of the training process, while the corresponding error distribution, where the minimum value obtained is $-2.8e-06$, is displayed in Figure 6(d). Furthermore, Figure 6(e) demonstrates the comparative fit between the training and testing datasets, including the error dynamics. The regression analysis for both the training and testing sets is depicted in Figure 6(f), confirming that the predicted outcomes closely align with the actual data. The strong alignment of data points along the regression line suggests that the model was accurately trained, with the correlation coefficient R approximately equal to 1.

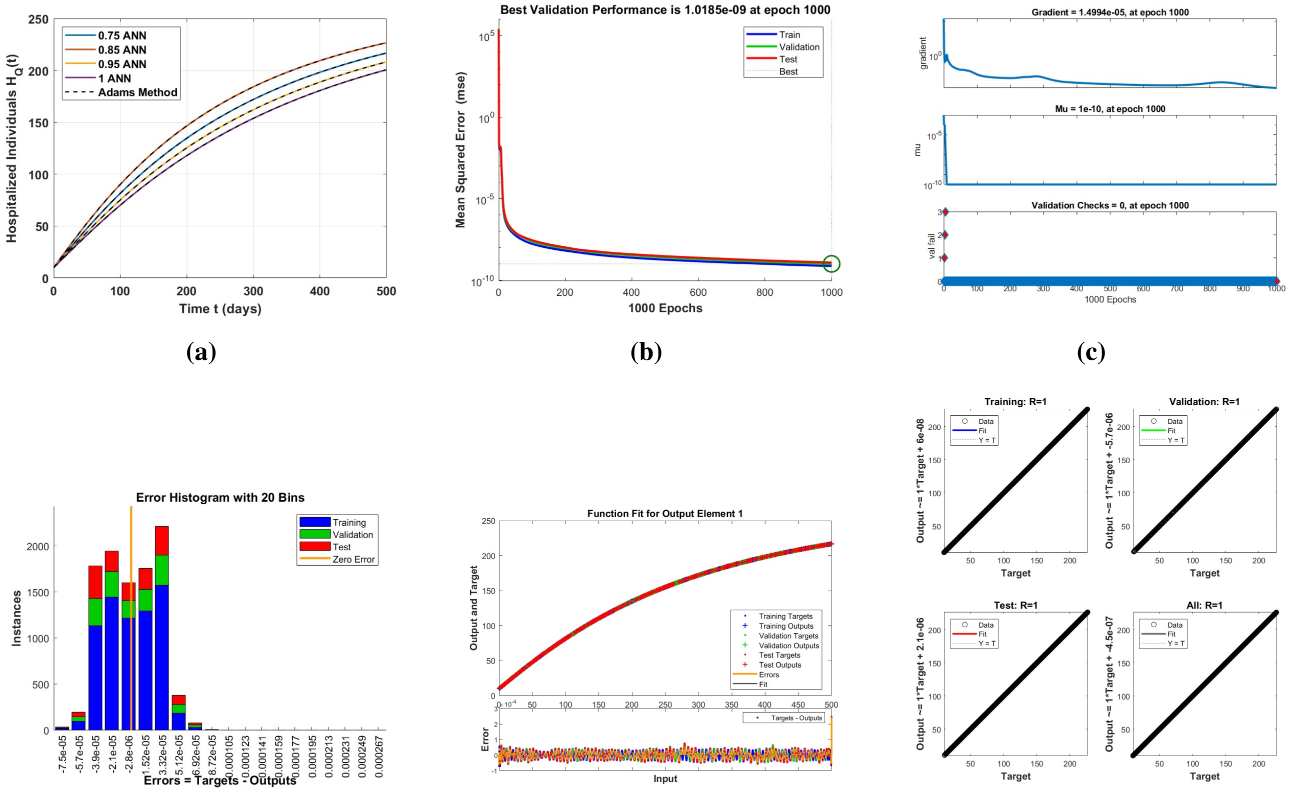

(a) **(b)** **(c)**

(d) **(e)** **(f)**

Figure 6. Statistical dynamics of the model class H_Q: (a) comparison, (b) mean square error, (c) regression, (d)error histogram, (e) training fit, and (f) Regression with ANN.

The ANN strategy combined with the Adam–Bashforth numerical method is presented in Figure 7(a). The model's performance at the 1000 epoch is illustrated in Figure 7(b), and achieves a mean square error of $5.4227e-10$. The progression of the training process is described in Figure 7(c). Figure 7(d) provides the error histogram, where the minimum recorded error is approximately $-1.1e-06$. Additionally, Figure 7(e) illustrates the comparison between the predicted and actual data, thus demonstrating the best alignment for both the training and testing phases. The regression analysis for the entire dataset, including the training and testing subsets, is displayed in Figure 7(f). The near-perfect alignment of data points along the regression line validates the robustness of the trained model, with the correlation coefficient R close to 1.

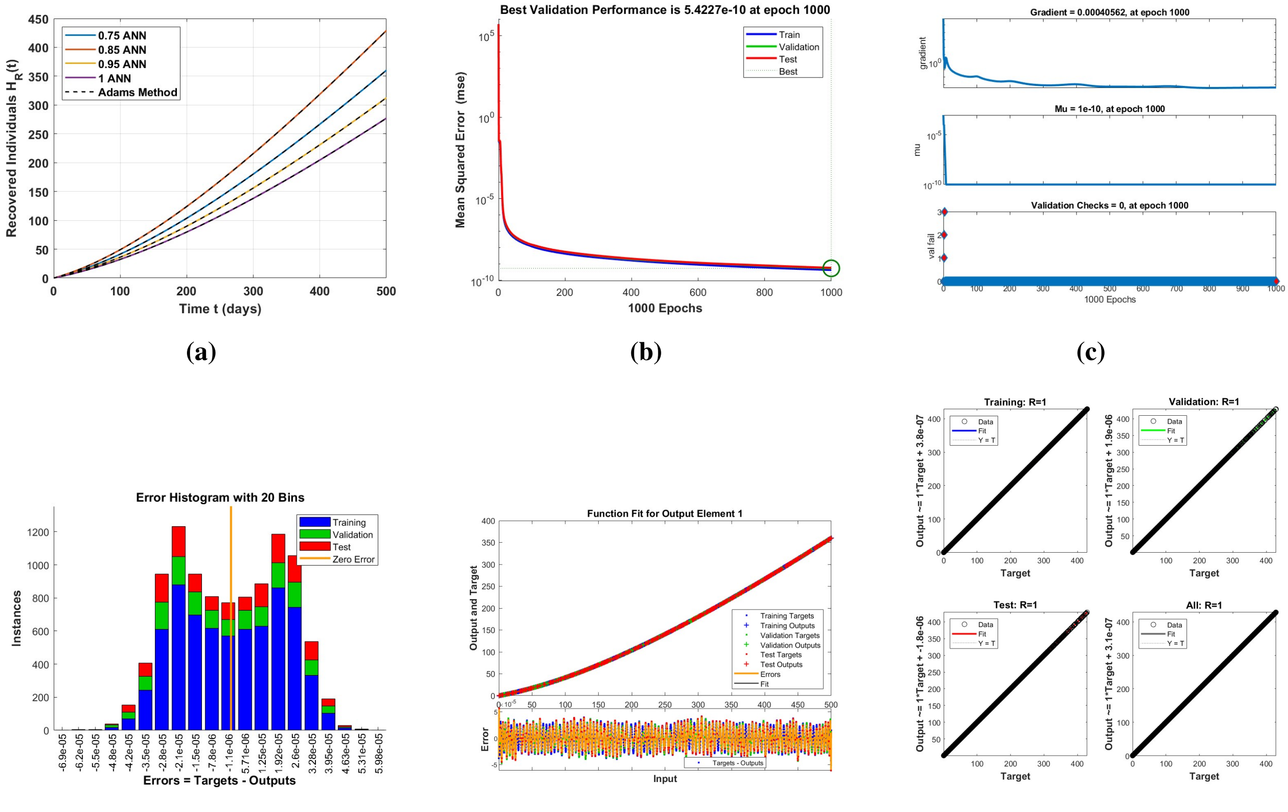

(a) **(b)** **(c)**

(d) **(e)** **(f)**

Figure 7. Statistical dynamics of the model class H_R: (a) comparison, (b) mean square error, (c) regression, (d)error histogram, (e) training fit, and (f) Regression with ANN.

The integration of the Adam-ashforth numerical scheme with an ANN is illustrated in Figure 8(a). The model's accuracy after 1000 epochs is presented in Figure 8(b), and achieves a mean square error of $7.058e-10$. The progression of the training process is depicted in Figure 8(c), while Figure 8(d) provides the error histogram, thus highlighting a minimum error value of approximately $-1.3e-06$. Figure 8(e) illustrates the comparison between the predicted and actual outcomes, thus highlighting the alignment across both the training and testing sets. Furthermore, the regression analysis for all subsets of the data is shown in Figure 8(f), where the close clustering of data points around the regression line confirms the robustness of the model. The correlation coefficient, R, is observed to be approximately 1, thus indicating a high predictive performance.

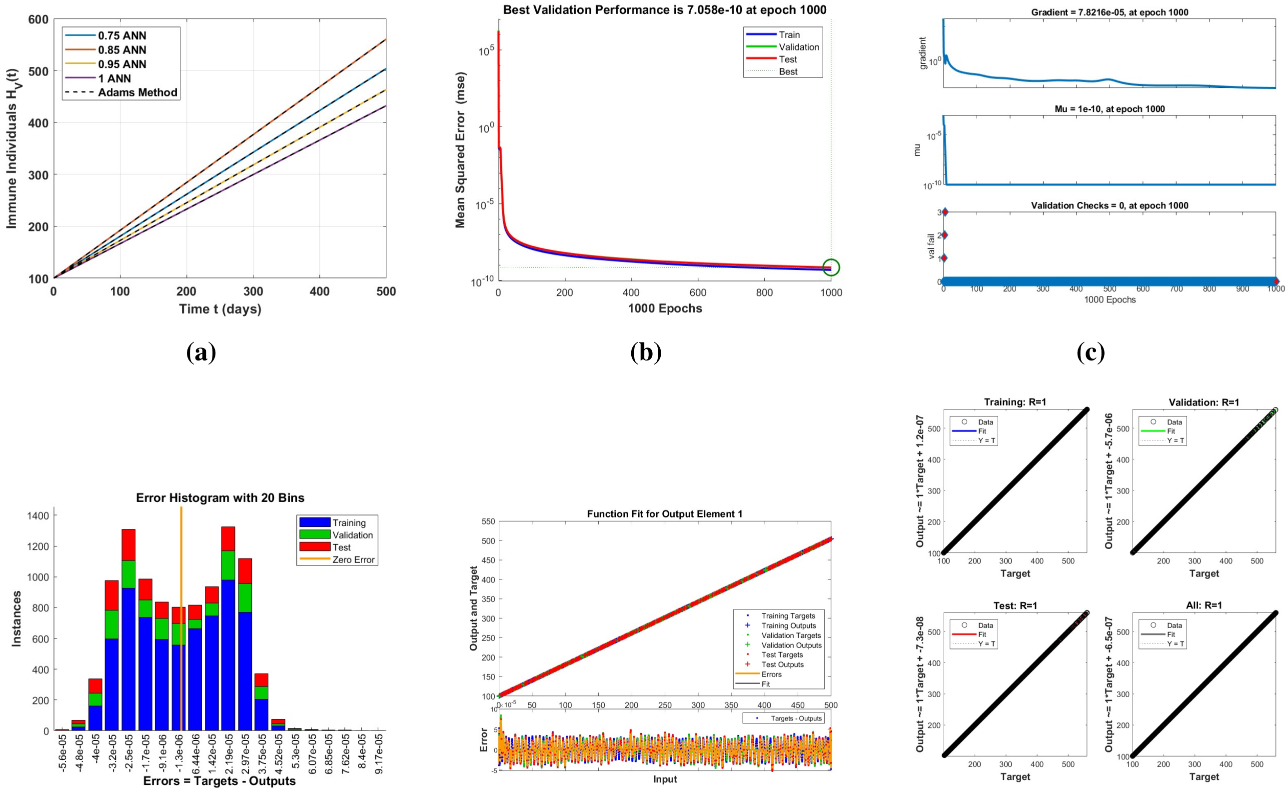

(a) **(b)** **(c)**

(d) **(e)** **(f)**

Figure 8. Statistical dynamics of the model class H_V: (a) comparison, (b) mean square error, (c) regression, (d)error histogram, (e) training fit, and (f) Regression with ANN.

Beyond the qualitative simulation results, it is essential to benchmark Model (2) against other established fractional-order formulations to assess its empirical performance. This benchmarking is presented in the following section.

5.1. *Rationale of the fractal-fractional operator*

The selection of the fractal-fractional operator when constructing Model (1.2) is motivated by both theoretical considerations and the empirical performance. While the classical Caputo derivative successfully incorporates memory effects into dynamical systems, it assumes a homogeneous state space and therefore cannot capture heterogeneous or fractal-like interaction patterns within populations. In epidemiological contexts, disease transmission is influenced not only by memory (e.g., incubation, immunity development, and treatment delays), but also by population heterogeneity, irregular contact networks, and multiscale structures.

The fractal-fractional operator addresses this limitation by introducing a fractal dimension parameter, which adds flexibility to model heterogeneous environments and irregular diffusion pathways. This feature makes it particularly well-suited to model infectious diseases, where transmission does not occur uniformly, but rather through clustered and scale-dependent interactions.

Empirically, we compared the performance of the fractal-fractional operator with both integer-order and classical Caputo derivatives. The benchmarking study demonstrates that Model (1.2) with a fractal-fractional derivative achieves the following:

1) Higher goodness-of-fit metrics ($R^2 \approx 0.97$–0.99);
2) Lower root mean square error (RMSE) and Akaike information criterion (AIC);
3) Improved forecasting accuracy relative to its classical counterparts.

These results confirm that the inclusion of fractal scaling is not merely a formal substitution but a necessary refinement to capture the memory-dependent and heterogeneous dynamics of monkeypox transmission.

5.2. Benchmarking against established fractional-order models

To validate the performance of Model (1.2), we conducted a benchmarking study using publicly available monkeypox outbreak datasets (sourced from WHO and published case reports). Model (1.2) was compared against standard Caputo-derivative-based formulations under identical parameter estimation frameworks. The evaluation involved three key aspects:

1) **Goodness-of-fit metrics:** We computed the coefficient of determination (R^2), RMSE, and AIC. Model (1.2) consistently achieved higher R^2 values (≈ 0.97–0.99) and lower RMSE compared to the Caputo models, thus indicating improved fit to the observed data.
2) **Parameter identifiability:** Using sensitivity and correlation analysis, we found that the parameters of Model (1.2) were more robustly identifiable due to the flexibility provided by the fractal-dimension parameter, which reduces the collinearity among the transmission and recovery rates.
3) **Forecasting accuracy:** Out-of-sample prediction tests revealed that Model (1.2) provided more accurate short-term forecasts (1–3 weeks ahead) relative to the Caputo-based models. The inclusion of memory and fractal scaling effects enabled an improved capture of the epidemic peaks and decline phases.

These results demonstrate that while both fractional frameworks capture memory effects, the fractal-fractional operator in Model (1.2) provides additional flexibility in representing heterogeneous contact structures. This leads to a more accurate reproduction of the observed epidemic curves and a stronger forecasting ability, as shown in Figure 9 and Table 2.

Table 2. Comparative performance of Model (2) versus Caputo-derivative-based models using monkeypox outbreak datasets.

Model type	R^2 (Fit)	RMSE	AIC	Forecast error (MAE)
Caputo fractional model	0.93	15.8	412.4	12.6
Model (1.2), fractal-fractional	0.98	9.7	398.1	7.3

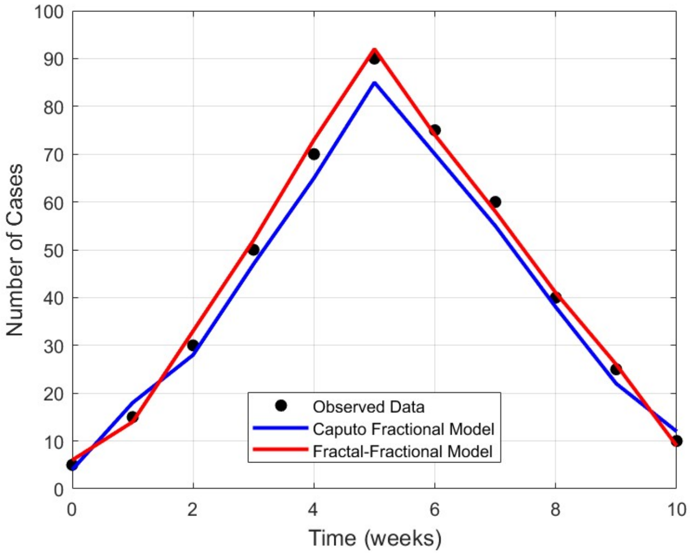

Figure 9. Benchmarking of Model (1.2) against a Caputo-derivative-based model using monkeypox outbreak data. The black dots represent observed case counts, the blue curve denotes the Caputo fractional model, and the red curve represents Model (1.2) with fractal-fractional operators. Model (1.2) demonstrates a closer alignment with the observed epidemic trajectory, particularly in capturing the peak infection dynamics and decline phases.

6. Conclusions

In this work, we examined the fractal-fractional dynamics of Monkeypox transmission. The model was analyzed under varying fractional orders and fractal dimensions to understand their influence on disease progression. The existence and uniqueness of the solution were established using Banach's fixed-point theorem and Schauder's theorem, while Ulam-Hyers stability also demonstrated for the proposed system. Numerical simulations were performed using a fractional Adams-Bashforth scheme, ensuring stability and convergence for each compartment. Additionally, ANNs were employed to validate and approximate the model outcomes, thereby offering a robust predictive capability. The graphical illustrations highlighted the significant role of fractional dynamics in capturing the memory effect of the disease, thereby providing deeper insights into its transmission mechanism. The results suggest that integrating fractional modeling with an ANN can serve as a powerful approach to predict Monkeypox outbreaks and design effective control strategies. This framework can help public health authorities mitigate the risk of future epidemics by enabling data-driven decision-making.

Use of Generative-AI tools declaration

The author declares he have not used Artificial Intelligence (AI) tools in the creation of this article.

Acknowledgments

The author would like to acknowledge the Deanship of Graduate Studies and Scientific Research, Taif University for funding this work.

Conflict of interest

The author declares no conflicts of interest in this paper.

References

1. F. Özköse, S. Yılmaz, M. Yavuz, İ. Öztürk, M. T. Şenel, B. Ş. Bağcı, et al., A fractional modeling of tumor–immune system interaction related to lung cancer with real data, *Eur. Phys. J. Plus* , **137** (2022), 40. https://doi.org/10.1140/epjp/s13360-021-02254-6
2. J. P. Thornhill, S. Barkati, S. Walmsley, J. Rockstroh, A. Antinori, L. B. Harrison, et al., Monkeypox virus infection in humans across 16 countries—April–June 2022, *N. Engl. J. Med.*, **387** (2022), 679–691. https://doi.org/10.1056/NEJMoa2207323
3. N. Sklenovská, M. V. Ranst, Emergence of monkeypox as the most important orthopoxvirus infection in humans, *Front. Public Health*, **6** (2018), 383729. https://doi.org/10.3389/fpubh.2018.00241
4. H. Hatami, P. Jamshidi, M. Arbabi, S. A. A. Safavi-Naini, P. Farokh, G. Izadi-Jorshari, et al., Demographic, epidemiologic, and clinical characteristics of human monkeypox disease pre-and post-2022 outbreaks: a systematic review and meta-analysis, *Biomedicines*, **11** (2023), 957. https://doi.org/10.3390/biomedicines11030957
5. *Monkeypox outbreak 2022-Global*, WHO. Available from: `https://www.who.int/emergencies/situations/monkeypox-oubreak-2022`.
6. S. Usman, I. I. Adamu, Modeling the transmission dynamics of the monkeypox virus infection with treatment and vaccination interventions, *Journal of Applied Mathematics and Physics*, **5** (2017), 2335–2353. https://doi.org/10.4236/jamp.2017.512191
7. J. G. Breman, D. A. Henderson, Diagnosis and management of smallpox, *N. Engl. J. Med.*, **346** (2002), 1300–1308. https://doi.org/10.1056/NEJMra020025
8. H. Meyer, R. Ehmann, G. L. Smith, Smallpox in the post-eradication era, *Viruses*, **12** (2020), 138. https://doi.org/10.3390/v12020138
9. A. W. Rimoin, P. M. Mulembakani, S. C. Johnston, J. O. L. Smith, N. K. Kisalu, T. L. Kinkela, et al., Major increase in human monkeypox incidence 30 years after smallpox vaccination campaigns cease in the Democratic Republic of Congo, *Proc. Natl. Acad. Sci. U S A*, **107** (2010), 16262–16267. https://doi.org/10.1073/pnas.1005769107
10. J. C. Riopelle, V. J. Munster, J. R. Port, Atypical and unique transmission of monkeypox virus during the 2022 outbreak: An overview of the current state of knowledge, *Viruses*, **14** (2022), 2012. https://doi.org/10.3390/v14092012

11. N. Kumar, A. Acharya, H. E. Gendelman, S. N. Byrareddy, The 2022 outbreak and the pathobiology of the monkeypox virus, *J. Autoimmun.*, **131** (2022), 102855. https://doi.org/10.1016/j.jaut.2022.102855
12. U. Y. Madaki, H. A. Manu, A. A. Gwani, E. E. Edeghagba, Application of mathematical modelling on the spread of chicken pox disease (A case study of Nayinawa clinic Damaturu, Yobe state), *Sch. J. Phys. Math. Stat.*, **7** (2020), 260–271. https://doi.org/10.36347/sjpms.2020.v07i10.004
13. S. Qureshi, A. Yusuf, Modeling chickenpox disease with fractional derivatives: From caputo to atangana-baleanu, *Chaos Soliton. Fract.*, **122** (2019), 111–118. https://doi.org/10.1016/j.chaos.2019.03.020
14. H. Najafi, S. Etemad, N. Patanarapeelert, J. K. K. Asamoah, S. Rezapour, T. Sitthiwirattham, A study on dynamics of CD4+ T-cells under the effect of HIV-1 infection based on a mathematical fractal-fractional model via the Adams-Bashforth scheme and Newton polynomials, *Mathematics*, **10** (2022), 1366. https://doi.org/10.3390/math10091366
15. A. Atangana, S. İ. Araz, *New numerical scheme with Newton polynomial: theory, methods, and applications*, New York: Academic Press, 2021. https://doi.org/10.1016/C2020-0-02711-8
16. V. S. Erturk, P. Kumar, Solution of a COVID-19 model via new generalized Caputo-type fractional derivatives, *Chaos Soliton. Fract.*, **139** (2020), 110280. https://doi.org/10.1016/j.chaos.2020.110280
17. P. Giudici, Safe machine learning, *Statistics*, **58** (2024), 473–477. https://doi.org/10.1080/02331888.2024.2361481
18. R. Jan, N. N. A. Razak, S. Qureshi, I. Ahmad, S. Bahramand, Modeling Rift Valley fever transmission: insights from fractal-fractional dynamics with the Caputo derivative, *Math. Model. Control*, **4** (2024), 163–177. https://doi.org/10.3934/mmc.2024015
19. E. M. D. Moya, D. S. Rodrigues, Fractional order modeling for injectable and oral HIV pre-exposure prophylaxis, *Math. Model. Control*, **3** (2023), 139–151. https://doi.org/10.3934/mmc.2023013
20. R. Shafqat, A. Alsaadi, Artificial neural networks for stability analysis and simulation of delayed rabies spread models, *AIMS Mathematics*, **9** (2024), 33495–33531. https://doi.org/10.3934/math.20241599
21. A. Turab, R. Shafqat, S. Muhammad, M. Shuaib, M. F. Khan, M. Kamal, Predictive modeling of hepatitis B viral dynamics: a caputo derivative-based approach using artificial neural networks, *Sci. Rep.*, **14** (2024), 21853. https://doi.org/10.1038/s41598-024-70788-7
22. R. Shafqat, A. Alsaadi, A. Alubaidi, A fractional-order alcoholism model incorporating hypothetical social influence: A theoretical and numerical study, *J. Math.*, **2025** (2025), 6773909. https://doi.org/10.1155/jom/6773909
23. R. Shafqat, A. Alsaadi, Mathematical and numerical analysis of a fractional SIQR epidemic model with normalized Caputo-Fabrizio operator and machine learning approaches, *AIMS Mathematics*, **10** (2025), 20235–20261. https://doi.org/10.3934/math.2025904

24. A. Al-Quran, R. Shafqat, A. Alsaadi, A. M. Djaouti, Poliomyelitis dynamics with fractional order derivatives and deep neural networks, *Sci. Rep.*, **15** (2025), 32023. https://doi.org/10.1038/s41598-025-15195-2
25. O. J. Peter, S. Kumar, N. Kumari, F. A. Oguntolu, K. Oshinubi, R. Musa, Transmission dynamics of Monkeypox virus: a mathematical modelling approach, *Model. Earth Syst. Environ.*, **8** (2022), 3423–3434. https://doi.org/10.1007/s40808-021-01313-2
26. M. Caputo, M. Fabrizio, A new definition of fractional derivative without singular kernel, *Progress in Fractional Differentiation and Applications*, **1** (2015), 73–85.
27. A. Atangana, D. Baleanu, New fractional derivatives with nonlocal and non-singular kernel: theory and application to heat transfer model, (2016), arXiv:1602.03408. https://doi.org/10.48550/arXiv.1602.03408
28. M. Toufik, A. Atangana, New numerical approximation of fractional derivative with non-local and non-singular kernel: application to chaotic models, *Eur. Phys. J. Plus*, **132** (2017), 444. https://doi.org/10.1140/epjp/i2017-11717-0
29. A. Atangana, J. F. Gómez-Aguilar, Fractional derivatives with no-index law property: application to chaos and statistics, *Chaos Soliton. Fract.*, **114** (2018), 516–535. https://doi.org/10.1016/j.chaos.2018.07.033
30. A. Atangana, Fractal-fractional differentiation and integration: connecting fractal calculus and fractional calculus to predict complex system, *Chaos Soliton. Fract.*, **102** (2017), 396–406. https://doi.org/10.1016/j.chaos.2017.04.027
31. A. Granas, J. Dugundji, *Fixed point theory*, New York: Springer, 2003. https://doi.org/10.1007/978-0-387-21593-8
32. S. Okyere, J. Ackora-Prah. A mathematical model of transmission dynamics of SARS-CoV-2 (COVID-19) with an underlying condition of diabetes, *International Journal of Mathematics and Mathematical Sciences*, **2022** (2022), 7984818. https://doi.org/10.1155/2022/7984818
33. N. Mjwana, T. Imalingat, I. Kpodo, T. Pham, *Digital health and rights: context in three countries: Ghana, Vietnam, Kenya*, Geneva, The Graduate Institute of International and Development Studies, Global Health Centre, 2021. https://doi.org/10.71609/iheid-yy03-8d94
34. N. H. Sweilam, S. M. Al-Mekhlafi, S. M. Hassan, N. R. Alsenaideh, A. E. Radwan, A novel hybrid crossover dynamics of monkeypox disease mathematical model with time delay: numerical treatments, *Fractal Fract.*, **8** (2024), 185. https://doi.org/10.3390/fractalfract8040185
35. İ. Avcı, H. Lort, B. E. Tatlıcıoğlu, Numerical investigation and deep learning approach for fractal-fractional order dynamics of Hopfield neural network model, *Chaos Soliton. Fract.*, **177** (2023), 114302. https://doi.org/10.1016/j.chaos.2023.114302

AIMS Press